Editors' Suggestion

Superconductivity in Compression-Shear Deformed Diamond

Chang Liu,[1] Xianqi Song,[1] Quan Li,[1,2,*] Yanming Ma,[1,2,†] and Changfeng Chen[3,‡]
[1]State Key Laboratory of Superhard Materials, Key Laboratory of Automobile Materials of MOE, Department of Materials Science, and Innovation Center for Computational Physics Method and Software, Jilin University, Changchun 130012, China
[2]International Center of Future Science, Jilin University, Changchun 130012, China
[3]Department of Physics and Astronomy, University of Nevada, Las Vegas, Nevada 89154, USA

(Received 11 October 2019; revised manuscript received 23 January 2020; accepted 3 March 2020; published 6 April 2020)

Diamond is a prototypical ultrawide band gap semiconductor, but turns into a superconductor with a critical temperature $T_c \approx 4$ K near 3% boron doping [E. A. Ekimov *et al.*, Nature (London) **428**, 542 (2004)]. Here we unveil a surprising new route to superconductivity in *undoped* diamond by compression-shear deformation that induces increasing metallization and lattice softening with rising strain, producing phonon mediated T_c up to 2.4–12.4 K for a wide range of Coulomb pseudopotential $\mu^* = 0.15$–0.05. This finding raises intriguing prospects of generating robust superconductivity in strained diamond crystal, showcasing a distinct and hitherto little explored approach to driving materials into superconducting states via strain engineering. These results hold promise for discovering superconductivity in normally nonsuperconductive materials, thereby expanding the landscape of viable nontraditional superconductors and offering actionable insights for experimental exploration.

DOI: 10.1103/PhysRevLett.124.147001

Diamond crystal comprises a carbon bonding network that produces superior mechanical strength and a very large electronic band gap at ambient conditions, making it a superstrong ultrawide band gap semiconductor. Theoretical studies predicted superconductivity in select semiconductors in the early 1960s [1,2], but superconducting states in technologically important group-IV semiconductors long eluded experimental detection. Ekimov *et al.* reported in 2004 synthesis of boron doped diamond with near 3% hole concentration, hosting a superconducting state with a critical temperature $T_c \approx 4$ K [3], and theoretical works [4–9] suggest an electron-phonon coupling mechanism. Similar phonon mediated superconductivity was later observed in silicon at 5.7–8.4 at.% boron doping, with a much lower T_c of 0.35 K due to weaker lattice vibration and reduced electron-phonon coupling [10] and in SiC at 2.2–3.9 at.% boron doping with a $T_c \approx 1.4$ K [11]. The discovery of superconductivity in these prominent semiconductors has prompted further explorations to advance fundamental understanding and potential innovative electronics applications [12,13].

Our recent studies show that diamond can be metallized under compression-shear (CS) deformation where a compressive stress prevents graphitization usually occurring in severely deformed diamond crystal [14]. This discovery raises intriguing prospects of intrinsic superconductivity in deformed diamond without external carrier doping. Here we report on a computational study of the evolution of electronic band structure, lattice vibration, and electron-phonon coupling along a typical deformation path where metallic states emerge and develop. We find that CS strains progressively enhance conduction electronic density of states near the Fermi energy and induce phonon softening in deformed diamond crystal. These effects combine to generate increasingly stronger electron-phonon coupling, driving diamond into a superconducting state. This phenomenon presents a distinct route toward intrinsic superconductivity in *undoped* diamond, expanding fundamental benchmarks of this prominent material. Our findings show that superconductivity may develop under complex strains in materials that are normally nonsuperconductive at ambient or simple pressure and stress conditions, opening a new area of research of hitherto largely unexplored *undoped* semiconductor-based superconductors. Such select deformation driven superconductivity is usually not accompanied by a conventional structural phase transition; instead, strain induced changes of bonding states and charge distribution in the deformed crystal generate concurrent electronic conduction and phonon softening that produce increasingly robust superconductivity. Recent experimental results show that strain modifies phonon modes in SrTiO3 films, resulting in enhanced superconducting transition temperatures, which suggests a promising approach to generating or enhancing superconductivity [15].

We have employed QUANTUM ESPRESSO (QE) code [16] for structural relaxation, stress-strain relation, and electronic band structure calculations based on the density functional theory (DFT) in the local density approximation (LDA) [17,18]. We also have performed lattice dynamics and electron-phonon coupling (EPC) calculations using the

density-functional perturbation theory (DFPT) in linear response as implemented in QE. Stress responses from QE calculations are in excellent agreement (less than 2% difference) with the results obtained from calculations using VASP code [19,20] with an energy convergence around 1 meV per atom and residual forces and stresses less than 0.005 eV Å^{-1} and 0.1 GPa, respectively. Electronic calculations adopted a kinetic energy cutoff of 100 Ry and a $16 \times 16 \times 24$ k mesh, and lattice dynamics calculations used a $4 \times 4 \times 6$ q mesh. LDA calculations tend to underestimate electronic band gap in semiconductors, but such calculations adequately describe metallic states and produce fairly accurate T_c in metallized semiconductors, e.g., in boron-doped diamond and silicon [3–10] and in MgB_2 [21–25]. Further computational details on consistency, convergence, and reliability tests are provided in the Supplemental Material [26].

From the Eliashberg theory of superconductivity [31,32], McMillan derived [33], later modified by Allen and Dynes [34], an analytic expression for transition temperature,

$$T_c = \frac{\omega_{\log}}{1.20} \exp\left\{ -\frac{1.04(1+\lambda)}{\lambda - \mu^*(1+0.62\lambda)} \right\}, \tag{1}$$

where $\omega_{\log}$ is a logarithmically averaged characteristic phonon frequency, and μ^* is the Coulomb pseudopotential that describes the effective electron-electron repulsion [35]. The ω-dependent EPC parameter $\lambda(\omega)$ is obtained from the Eliashberg spectral function $\alpha^2F(\omega)$,

$$\lambda(\omega) = 2\int_0^{\omega} \frac{\alpha^2F(\omega)}{\omega} d\omega, \tag{2}$$

with $\lambda(\infty)$ giving the total EPC parameter λ in the T_c equation, and

$$\alpha^2F(\omega) = \frac{1}{2}\sum_j \int_{\mathrm{BZ}} \frac{d\boldsymbol{q}}{\Omega_{\mathrm{BZ}}} \omega_{\boldsymbol{q}j}\lambda_{\boldsymbol{q}j}\delta(\omega - \omega_{\boldsymbol{q}j}). \tag{3}$$

Here, the integration is done over the Brillouin zone (BZ) of volume Ω_{BZ}, and EPC parameter for mode j at wave vector $\boldsymbol{q}$ is $\lambda_{\boldsymbol{q}j} = \gamma_{\boldsymbol{q}j}/\pi\hbar N_F\omega_{\boldsymbol{q}j}^2$, where $\gamma_{\boldsymbol{q}j} = 2\pi\omega_{\boldsymbol{q}j}\sum_{nm}\int_{\mathrm{BZ}}[(d\boldsymbol{k})/(\Omega_{\mathrm{BZ}})]|g^j_{\boldsymbol{k}n,\boldsymbol{k}+\boldsymbol{q}m}|^2\delta(\varepsilon_{\boldsymbol{k}n}-\varepsilon_F)\delta(\varepsilon_{\boldsymbol{k}+\boldsymbol{q}m}-\varepsilon_F)$ is the linewidth for mode j at wave vector q, arising from electron-phonon coupling, $\varepsilon_{\boldsymbol{k}n}$ is the band energy at $\boldsymbol{k}$, and the electron-phonon interaction matrix element is

$$g^j_{\boldsymbol{k}n,\boldsymbol{k}+\boldsymbol{q}m} = \sqrt{\frac{\hbar}{2M\omega_{\boldsymbol{q}j}}}\langle\varphi_{\boldsymbol{k}n}|\nabla V_{\boldsymbol{q}}\cdot\boldsymbol{e}_{\boldsymbol{q}j}|\varphi_{\boldsymbol{k}+\boldsymbol{q}m}\rangle, \tag{4}$$

where M is the ionic mass, $\nabla V_{\boldsymbol{q}}$ is the gradient of crystal potential with respect to ionic displacements, and $\boldsymbol{e}_{\boldsymbol{q}j}$ is the polarization vector of phonon mode j at wave vector $\boldsymbol{q}$.

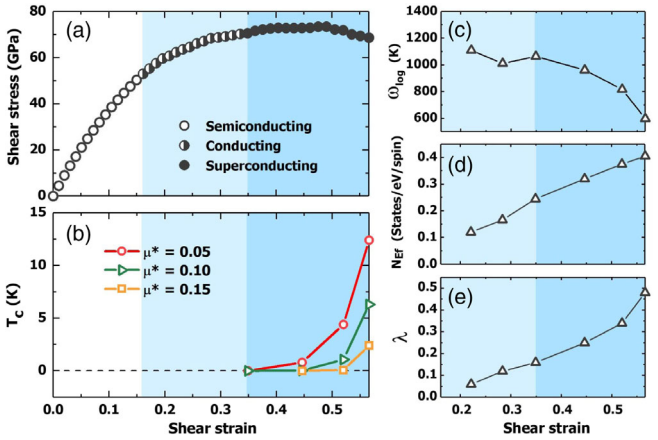

FIG. 1. (a) The semiconducting, conducting, and superconducting stages of electronic evolution in deformed diamond indicated on the (11-2)[111] CS stress-strain curve. (b) Strain dependence of T_c for a selected range of μ^*. (c)–(e) Strain evolution of logarithmically averaged phonon frequency $\omega_{\log}$, electronic density of states at the Fermi energy N_{E_F}, and electron-phonon coupling parameter λ.

The Allen-Dynes modified McMillan T_c equation is widely adopted and generally accurate for materials with $\lambda < 1.5$ [36–39], whereas a numerical solution to the Eliashberg equation [31] is more adequate at larger λ as in, e.g., high-T_c superconducting superhydrides [40,41]. The interaction between electrons is commonly described by the Coulomb pseudopotential μ^*, which can be obtained from an inversion process by fitting experimental single-particle tunneling data [36–38], and is often treated as an adjustable parameter. The values of μ^* mostly stay within a very narrow range around 0.1 for most materials, making this formulism highly robust [34–39]. Pertinent examples include works on MgB_2 and boron-doped diamond and silicon that all adopted $\mu^* \sim 0.10$ (0.08–0.13, mostly set to 0.10), producing T_c in good agreement with measured data [4,5,10,21–25]. The robustness of this approach is also verified by the latest *ab initio* Eliashberg theory calculations that map out effective μ^* by fitting Eq. (1) to the fully solved Eliashberg T_c [39]. Smaller values of μ^* also occur, like $\mu^* = 0.06$ for a high-pressure phase of Si [42]. In this work, we select a relatively broad range of $\mu^* = 0.05$–0.15 for deformed diamond, which hosts strain-dependent electronic states thus changing electronic interactions, making the ranged μ^* a well-suited choice.

We explore mechanical deformation induced superconductivity, focusing on diamond under (11-2)[111] CS strain, which exhibits representative structural and electronic behaviors under CS strains. At increasing strains, we closely examine (i) evolutions of electronic bands and the associated variations in bonding and conduction charge distribution and (ii) phonon softening patterns and rising electron-phonon coupling in the deformed diamond crystal. We present in Fig. 1 our main findings on the emergence of

superconductivity in progressively deformed diamond, which goes through three distinct stages under CS strains. In the first stage, the electronic band gap gradually decreases with increasing deformation and comes to a complete closure at CS strain $\epsilon \approx 0.161$ [43]. The second stage develops at further increasing strains, with rising accumulation of electronic states near the Fermi energy, but electronic density of states (EDOS) and EPC are too weak to produce an appreciable superconducting state. Superconductivity occurs in the third stage well inside the metallic regime at CS strain $\epsilon \approx 0.349$ where a sufficiently high EDOS has been reached and, perhaps more significant, the deformed diamond lattice softens considerably to generate a strong EPC (see below). This process leads to a rising CS-strain driven T_c that reaches 2.4–12.4 K for Coulomb pseudopotential $\mu^* = 0.15$–0.05. These surprisingly high T_c values under realistic μ^* place deformed diamond among the most prominent elemental superconductors [44].

To decipher key factors driving CS deformed diamond into a superconducting state, we first examine evolution of electronic states, focusing on changes in bonding charge and emergence of conduction charge. The electronic band structures and the corresponding EDOS of deformed diamond at selected strains are shown in Fig. 2. It is seen that band states start to cross the Fermi level around shear strain 0.161, and an increasing number of bands and amount of states pass the Fermi level at higher strains, generating a rising EDOS (N_{E_F}) at the Fermi energy. At shear strain 0.349, N_{E_F} reaches a level comparable to those in boron-doped diamond and Si [4,5], initiating an appreciable superconducting state [Figs. 1(a) and 1(b)]. Accumulated electronic states distribute smoothly around the Fermi level, conforming to near-constant EDOS close to E_F required for the derivation of many equations [37,38], including Eqs. (1)–(4). In Fig. 2(e), we show total charge in minimally ($\epsilon = 0.000$) and maximally ($\epsilon = 0.566$) strained stable diamond structures. A significant depletion of bonding charge is seen in the latter case, which weakens C-C bonds, especially those aligned in the [111] and [11-1] directions. To track strain induced charge redistribution, particularly their contribution toward conduction, we integrated EDOS in the $[-0.3, 0.3]$ eV energy window around the Fermi level, and the resulting conduction charge patterns are plotted in Fig. 2(f), where both a local view (left panel) and extended view (right panel) are shown. Conduction charges center on carbon atoms between bonds that span a large angular space driven by CS strains, and point away from all C-C bonds in the crystal. The extended view further highlights that conduction charges locate in buckled (111) and (11-1) planes separated by the deformation weakened [111] and [11-1] bonds. This pattern of nonbonding conduction charge is similar to that in graphite, where nonbonding π states in the graphitic sheets contribute to electrical conduction. It is noted, however, the bulk bonding network remains intact without graphitization in CS

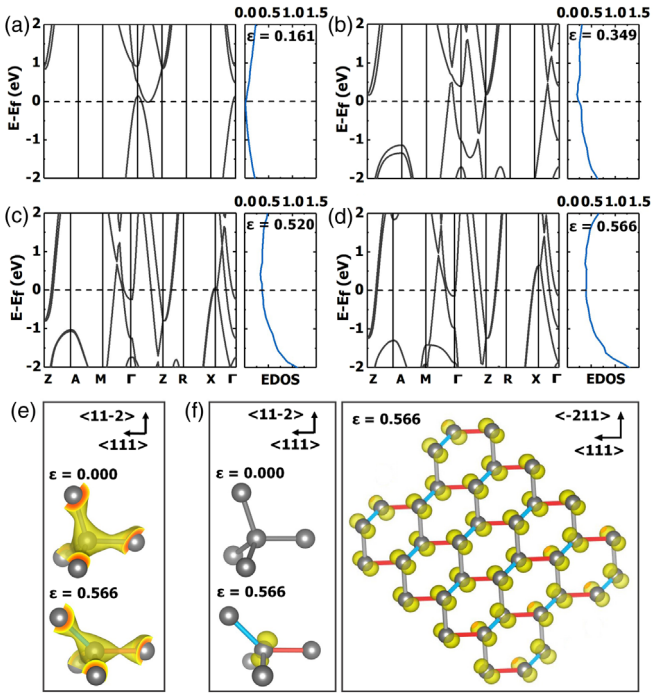

FIG. 2. (a)–(d) Electronic band structure and density of states (EDOS, in states/eV/spin) at selected CS strains. (e) Tetrahedrally bonded structural unit with total charge in stable diamond lattice at minimal ($\epsilon = 0.000$) and maximal ($\epsilon = 0.566$) CS strains in the indicated crystallographic direction. (f) Left panel: a local view of conduction charge distribution from integrated EDOS in $[-0.3, 0.3]$ eV around the Fermi level at $\epsilon = 0.000$ and 0.566 along the indicated crystallographic orientation; right panel: the same charge distribution presented in an extended view to showcase the global pattern of conduction charge in crystal planes relative to the strain weakened bonds in the [111] (marked red) and [11-1] (blue) directions.

deformed diamond. The EDOS values at large CS strains, e.g., 0.520 and 0.566, are considerably higher than in boron-doped diamond and silicon [4,5], which should produce better screening thus smaller μ^* in CS strained diamond than previously reported 0.10 [4,5], suggesting T_c of deformed diamond should reach the upper range shown in Fig. 1(b).

We next explore lattice dynamics of deformed diamond and assess the evolution of phonon spectra and the associated EPC with rising strains. Plotted in Figs. 3(a)–3(d) are calculated phonon dispersion curves and the corresponding spectral function $\alpha^2F(\omega)/\omega$ and EPC parameter $\lambda(\omega)$ at selected strains. Several spectral features are noteworthy. There is an overall spectral softening as increasing strains, reflecting a general weakening of deformed C-C bonds under CS strains, which explains the decrease of logarithmically averaged phonon frequency $\omega_{\log}$ in the superconducting regime as shown in Fig. 1(c). There is an especially pronounced phonon softening at A in the Brillouin zone as seen in Figs. 3(a)–3(d), where a large drop of frequency occurs concomitantly with a significant increase of EPC, resulting in a steep rise of $\lambda(\omega)$ in the corresponding

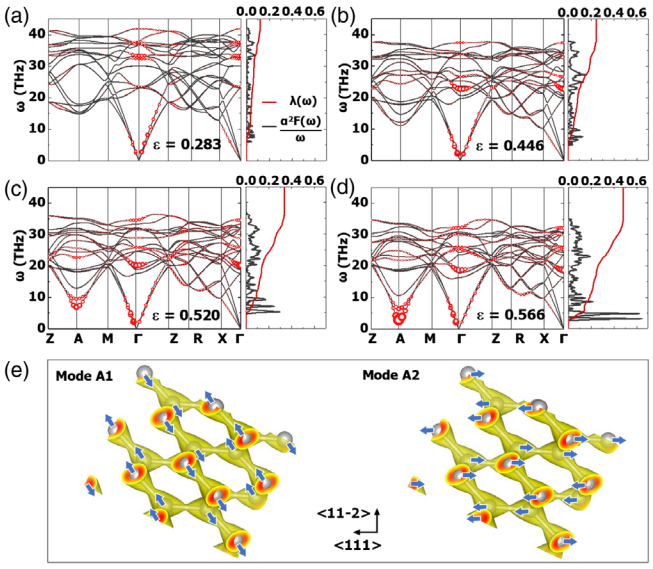

FIG. 3. (a)–(d) Phonon dispersion curves with the strength of q-resolved EPC parameter λ_q, indicated by the size of red circles (left panels) and spectral function $\alpha^2F(\omega)/\omega$ and $\lambda(\omega)$ (right panels) at selected strains. (e) Vibrational modes of the two lowest-frequency branches at A, modes $A1$ and $A2$, at CS strain $\epsilon = 0.566$ with polarization vectors $\boldsymbol{e}_{qj}$ pointed in the [11-1] and [111] directions as indicated by the arrows, which are aligned with the most charge depleted bonds that set the directions of the crystal potential gradients ∇V_q.

low-frequency range. To elucidate the underlying mechanism, we show in Fig. 3(e) the vibrational modes of the two lowest-frequency phonon branches at A, labeled mode $A1$ and mode $A2$, which exhibit the most profound CS strain induced softening. These phonon modes correspond to relative shear oscillations of the (111) and (11-1) crystal planes connected by the charge-depletion weakened bonds, which explains the pronounced reduction of the associated phonon frequency. Moreover, the directions of the polarization $\boldsymbol{e}_{qj}$ of these phonon modes, as indicated by the arrows, are aligned with the charge-depleted [111] and [11-1] bonds, respectively. Since charge depletion occurs mostly in the middle of these weakened bonds, the resulting charge disparities along these bonds produce large magnitudes for the gradients of the crystal potential ∇V_q aligned in the same directions as those of $\boldsymbol{e}_{qj}$. As such, the $\nabla V_q \cdot \boldsymbol{e}_{qj}$ term in the matrix element in Eq. (4) is maximally optimized, accounting for the greatly enhanced EPC. These results showcase an effective strain altered charge redistribution in the deformed crystal lattice that plays the dual role of softening phonon modes and enhancing EPC, and this may be a robust mechanism in a broad range of materials, offering crucial guiding principles in search of strain engineered nontraditional superconductors.

Further studies of aspects not considered in this work, e.g., the anharmonic phonon effect and EPC anisotropy, may offer insights for more accurate understanding of superconducting diamond; also of interest are thermodynamic properties that can be derived from numerically solving the full Eliashberg equation. Anisotropic EPC has been shown to enhance T_c considerably in MgB_2 [25], and such an effect would strengthen our reported results. A major complication in studying boron-doped diamond, Si, and SiC is structural disorder introduced by the doping process [12]. In contrast, *undoped* CS deformed diamond provides a platform for exploring intrinsic superconductivity in a metallized semiconductor, and this phenomenon may be prevalent among many semiconductors, suggesting a promising new research area of fundamental and practical significance. Our results also hold major implications for high-pressure experiments using diamond anvil cells (DAC), whose culet regions hosting four-probe leads for transport measurements commonly experience large pressure gradients with considerable CS strains [45]. At extreme loadings these regions may become superconducting and impede measurements probing superconductivity in specimens inside the DAC chamber. Meticulous measurements should verify this intriguing phenomenon. It is noted that the predicted superconductivity in deformed diamond occurs in a strain range near ductile failure. The newly identified compression-shear mode [14], however, offers an effective channel for releasing stress and energy thus sustaining the structural integrity in the deformation regime of a flat stress-strain curve. This new mechanism results in a significantly reduced overall bond elongation under CS, leading to a much-reduced rate of stress and energy increase with rising strains, in stark contrast to the uniaxial case. Moreover, loaded DAC contains small regions with high CS stresses surrounded by much larger less-stressed volumes [46]. This setting helps contain the severely CS deformed region, preventing any runaway structural failure. Similar situations exist in rotational DAC [47] and manipulated nanoscale diamond [48,49], where the largest CS deformed region is surrounded and supported by less-deformed crystal structure or other confining device components, thereby making the CS deformed superconducting region viable and accessible to experimental probes.

In summary, we have uncovered a new route to superconductivity in diamond by mechanical deformation. Compression-shear strained diamond crystal hosts deformed bonds with significant charge depletion, facilitating a buildup of conduction charge in crystal planes separated by the depletion-weakened bonds. At large strains well inside the metallic regime, superconductivity emerges at increasing accumulation of conduction states at the Fermi energy and progressively more pronounced softening of phonon modes, especially the shear modes associated with the most severely deformation-weakened bonds. These effects together produce increasingly stronger electron-phonon coupling, leading to rising superconducting transition temperature T_c that reaches 2.4–12.4 K for a

broad range of Coulomb pseudopotentials $\mu^* = 0.15$–0.05. These results place deformed diamond among prominently select elemental solids that exhibit the highest T_c values. The present work raises exciting prospects of turning normally nonsuperconductive materials into intrinsic superconductors by a hitherto little explored strain engineering approach, which holds promise for finding a distinct class of deformation driven nontraditional superconductors.

This research was supported by the National Key Research and Development Program of China under Grant No. 2018YFA0703404, the Natural Science Foundation of China under Grants No. 11622432, No. 11474125, and No. 11534003, and Program for JLU Science and Technology Innovative Research Team.

*liquan777@calypso.cn
†mym@jlu.edu.cn
‡chen@physics.unlv.edu

[1] V. L. Gurevich, A. I. Larkin, and Y. A. Firsov, On the possibility of superconductivity in semiconductors, Sov. Phys. Solid State **4**, 131 (1962).
[2] M. L. Cohen, Superconductivity in many-valley semiconductors and in semimetals, Phys. Rev. **134**, A511 (1964).
[3] E. A. Ekimov, V. A. Sidorov, E. D. Bauer, N. N. Melnik, N. J. Curro, J. D. Thompson, and S. M. Stishov, Superconductivity in diamond, Nature (London) **428**, 542 (2004).
[4] L. Boeri, J. Kortus, and O. K. Andersen, Three-Dimensional MgB_2-Type Superconductivity in Hole-Doped Diamond, Phys. Rev. Lett. **93**, 237002 (2004).
[5] K.-W. Lee and W. E. Pickett, Superconductivity in Boron-Doped Diamond, Phys. Rev. Lett. **93**, 237003 (2004).
[6] H. J. Xiang, Z. Y. Li, J. L. Yang, J. G. Hou, and Q. S. Zhu, Electron-phonon coupling in a boron-doped diamond superconductor, Phys. Rev. B **70**, 212504 (2004).
[7] X. Blase, Ch. Adessi, and D. Connetable, Role of the Dopant in the Superconductivity of Diamond, Phys. Rev. Lett. **93**, 237004 (2004).
[8] Y. Ma, J. S. Tse, T. Cui, D. D. Klug, L. Zhang, Y. Xie, Y. Niu, and G. Zou, First-principles study of electron-phonon coupling in hole- and electron-doped diamonds in the virtual crystal approximation, Phys. Rev. B **72**, 014306 (2005).
[9] F. Giustino, J. R. Yates, I. Souza, M. L. Cohen, and S. G. Louie, Electron-Phonon Interaction via Electronic and Lattice Wannier Functions: Superconductivity in Boron-Doped Diamond Reexamined, Phys. Rev. Lett. **98**, 047005 (2007).
[10] E. Bustarret, C. Marcenat, P. Achatz, J. Kacmarcik, F. Levy, A. Huxley, L. Ortega, E. Bourgeois, X. Blase, D. Debarre, and J. Boulmer, Superconductivity in doped cubic silicon, Nature (London) **444**, 465 (2006).
[11] Z. A. Ren, J. Kato, T. Muranaka, J. Akimitsu, M. Kriener, and Y. Maeno, Superconductivity in Boron-doped SiC, J. Phys. Soc. Jpn. **76**, 103710 (2007).
[12] X. Blase, E. Bustarret, C. Chapelier, T. Klein, and C. Marcenat, Superconducting group-IV semiconductors, Nat. Mater. **8**, 375 (2009).
[13] E. Bustarret, Superconductivity in doped semiconductors, Physica (Amsterdam) **514C**, 36 (2015).
[14] C. Liu, X. Q. Song, Q. Li, Y. M. Ma, and C. F. Chen, Smooth Flow in Diamond: Atomistic Ductility and Electronic Conductivity, Phys. Rev. Lett. **123**, 195504 (2019).
[15] K. Ahadi, L. Galletti, Y. Li, S. Salmani-Rezaie, W. Wu, and S. Stemmer, Enhancing superconductivity in $SrTiO_3$ films with strain, Sci. Adv. **5**, eaaw0120 (2019).
[16] P. Giannozzi *et al.*, Quantum Espresso: A modular and open-source software project for quantum simulations of materials, J. Phys. Condens. Matter **21**, 395502 (2009).
[17] J. P. Perdew and A. Zunger, Self-interaction correction to density-functional approximations for many-electron systems, Phys. Rev. B **23**, 5048 (1981).
[18] D. M. Ceperley and B. J. Alder, Ground State of the Electron Gas by a Stochastic Method, Phys. Rev. Lett. **45**, 566 (1980).
[19] G. Kresse and L. Furthmüller, Efficient iterative schemes for ab initio total-energy calculations using a plane-wave basis set, Phys. Rev. B **54**, 11169 (1996).
[20] G. Kresse and D. Joubert, From ultrasoft pseudopotentials to the projector augmented-wave method, Phys. Rev. B **59**, 1758 (1999).
[21] J. M. An and W. E. Pickett, Superconductivity of MgB_2: Covalent Bonds Driven Metallic, Phys. Rev. Lett. **86**, 4366 (2001).
[22] A. Y. Liu, I. I. Mazin, and J. Kortus, Beyond Eliashberg Superconductivity in MgB_2: Anharmonicity, Two-Phonon Scattering, and Multiple Gaps, Phys. Rev. Lett. **87**, 087005 (2001).
[23] J. Kortus, I. I. Mazin, K. D. Belashchenko, V. P. Antropov, and L. L. Boyer, Superconductivity of Metallic Boron in MgB_2, Phys. Rev. Lett. **86**, 4656 (2001).
[24] Y. Kong, O. V. Dolgov, O. Jepsen, and O. K. Andersen, Electron-phonon interaction in the normal and superconducting states of MgB_2, Phys. Rev. B **64**, 020501(R) (2001).
[25] H. J. Choi, D. Roundy, H. Sun, M. L. Cohen, and S. G. Louie, First-principles calculation of the superconducting transition in MgB_2 within the anisotropic Eliashberg formalism, Phys. Rev. B **66**, 020513(R) (2002).
[26] See Supplemental Material at http://link.aps.org/supplemental/10.1103/PhysRevLett.124.147001 for further computational details on consistency, convergence, and reliability tests to validate and support the reported results, which includes Refs. [27–30].
[27] E. S. Zouboulis, M. Grimsditch, A. K. Ramdas, and S. Rodriguez, Temperature dependence of the elastic moduli of diamond: A Brillouin-scattering study, Phys. Rev. B **57**, 2889 (1998).
[28] D. M. Teter, Computational alchemy: The search for new superhard materials, MRS Bull. **23**, 22 (1998).
[29] J. P. Perdew, K. Burke, and M. Ernzerhof, Generalized Gradient Approximation Made Simple, Phys. Rev. Lett. **77**, 3865 (1996).
[30] J. Heyd, G. E. Scuseria, and M. Ernzerhof, Hybrid functionals based on a screened Coulomb potential, J. Chem. Phys. **118**, 8207 (2003).
[31] G. M. Eliashberg, Interactions between electrons and lattice vibrations in a superconductor, Sov. Phys. JETP **11**, 696 (1960).

[32] D. J. Scalapino, J. R. Schrieffer, and J. W. Wilkins, Strong-coupling superconductivity. I, Phys. Rev. **148**, 263 (1966).
[33] W. L. McMillan, Transition temperature of strong-coupled superconductor, Phys. Rev. **167**, 331 (1968).
[34] P. B. Allen and R. C. Dynes, Transition temperature of strong-coupled superconductors reanalyzed, Phys. Rev. B **12**, 905 (1975).
[35] P. Morel and P. W. Anderson, Calculation of the superconducting state parameters with retarded electron-phonon interaction, Phys. Rev. **125**, 1263 (1962).
[36] W. L. McMillan and J. M. Rowell, in *Superconductivity*, edited by R. D. Parks (Marcel Dekker, New York, 1969), Vol. 1, p. 561.
[37] J. P. Carbotte, Properties of boson-exchange superconductivity, Rev. Mod. Phys. **62**, 1027 (1990).
[38] J. P. Carbotte and F. Marsiglio, Electron-phonon superconductivity, in *Superconductivity*, edited by K. H. Bennemann and J. B. Ketterson, The Physics of Superconductors (Springer, Berlin, Heidelberg, 2003).
[39] A. Sanna, J. A. Flores-Livas, A. Davydov, G. Profeta, K. Dewhurst, S. Sharma1, and E. K. U. Gross, Ab initio Eliashberg theory: Making genuine predictions of superconducting features, J. Phys. Soc. Jpn. **87**, 041012 (2018).
[40] F. Peng, Y. Sun, C. J. Pickard, R. J. Needs, Q. Wu, and Y. M. Ma, Hydrogen Clathrate Structures in Rare Earth Hydrides at High Pressures: Possible Route to Room-Temperature Superconductivity, Phys. Rev. Lett. **119**, 107001 (2017).
[41] Y. Sun, J. Lv, Y. Xie, H. Liu, and Y. M. Ma, Route to a Superconducting Phase above Room Temperature in Electron-Doped Hydride Compounds under High Pressure, Phys. Rev. Lett. **123**, 097001 (2019).
[42] K. J. Chang, M. M. Dacorogna, M. L. Cohen, J. M. Mignot, G. Chouteau, and G. Martinez, Superconductivity in High-Pressure Metallic Phases of Si, Phys. Rev. Lett. **54**, 2375 (1985).
[43] For consistency, all computational results reported here are obtained from LDA calculations that are adopted in the QE code for lattice dynamics and electron-phonon coupling calculations. It should be noted that LDA underestimates the band gap compared to the more accurate band gap values from using the HSE functional as previously reported [14], resulting in a small ($\approx$0.06) downshift of strain where metallization indicated by the band gap closure occurs. This strain downshift, however, does not impact the main conclusions and underlying physics mechanisms presented and discussed in this Letter.
[44] G. W. Webb, F. Marsiglio, and J. E. Hirsch, Superconductivity in the elements, alloys and simple compounds, Physica (Amsterdam) **514C**, 17 (2015).
[45] B. Li, C. Ji, W. Yang, J. Wang, K. Yang, R. Xu, W. Liu, Z. Cai, J. Chen, and H. K. Mao, Diamond anvil cell behavior up to 4 Mbar, Proc. Natl. Acad. Sci. U.S.A. **115**, 1713 (2018).
[46] A. L. Ruoff and H. Luo, Pressure strengthening: A possible route to obtaining 9 Mbar and metallic diamonds, J. Appl. Phys. **70**, 2066 (1991).
[47] C. Ji, V. I. Levitas, H. Zhu, J. Chaudhuri, A. Marathe, and Y. Ma, Shear-induced phase transition of nanocrystalline hexagonal boron nitride to wurtzitic structure at room temperature and lower pressure, Proc. Natl. Acad. Sci. U.S.A. **109**, 19108 (2012).
[48] A. Banerjee, D. Bernoulli, H. Zhang1, M. F. Yuen, J. Liu, J. Dong, F. Ding, J. Lu, M. Dao, W. Zhang, Y. Lu, and S. Suresh, Ultralarge elastic deformation of nanoscale diamond, Science **360**, 300 (2018).
[49] A. Nie, Y. Bu, P. Li, Y. Zhang, T. Jin, J. Liu, Z. Su, Y. Wang, J. He, Z. Liu, H. Wang, Y. Tian, and W. Yang, Approaching diamonds theoretical elasticity and strength limits, Nat. Commun. **10**, 5533 (2019).

Supplemental Material on

Superconductivity in Compression-Shear Deformed Diamond

Chang Liu[1], Xianqi Song[1], Quan Li [1,2], Yanming Ma[1,2], and Changfeng Chen[3]

[1]*State Key Laboratory of Superhard Materials, Key Laboratory of Automobile Materials of MOE, Department of Materials Science, and Innovation Center for Computational Physics Method and Software, Jilin University, Changchun 130012, China.*

[2]*International Center of Future Science, Jilin University, Changchun 130012, China.*

[3]*Department of Physics and Astronomy, University of Nevada, Las Vegas, Nevada 89154, USA.*

Here we provide supplemental details on the consistency, convergence, and numerical reliability of our reported results. Specifically, this document contains the following: (1) Table S1 showing that LDA and GGA results are consistent with experimental data on diamond, (2) Figure S1 showing that the stress-strain relation is insensitive to the choice of the exchange-correlation functional (LDA and GGA), (3) Figure S2 showing a comparison of the calculated LDA and HSE band gap, (4) Figure S3 showing the q-mesh convergence test result, (5) Figure S4 showing the energy barrier for atomic movements along the path of vibrational eigenstates of the A-point phonon modes.

Table S1 Calculated lattice parameters a_0 (Å), elastic constants C_{ij} (GPa), bulk modulus B (GPa) and shear modulus G (GPa) using the LDA or GGA functional compared with experimental data of diamond.

	a_0	C_{11}	C_{12}	C_{44}	B	G
GGA	3.572	1053.0	126.2	562.4	435.2	520.5
LDA	3.534	1102.8	149.5	597.5	467.2	545.8
Exp.	3.567[a]	1080.4[a]	127.0[a]	576.6[a]	443.0[b]	535.0[b]

[a] Reference [1]

[b] Reference [2]

The lattice parameters, elastic constants, and bulk and shear modulus calculated using the local density approximation (LDA) [3] and generalized gradient approximation (GGA) [4] are in good agreement with experimental data.

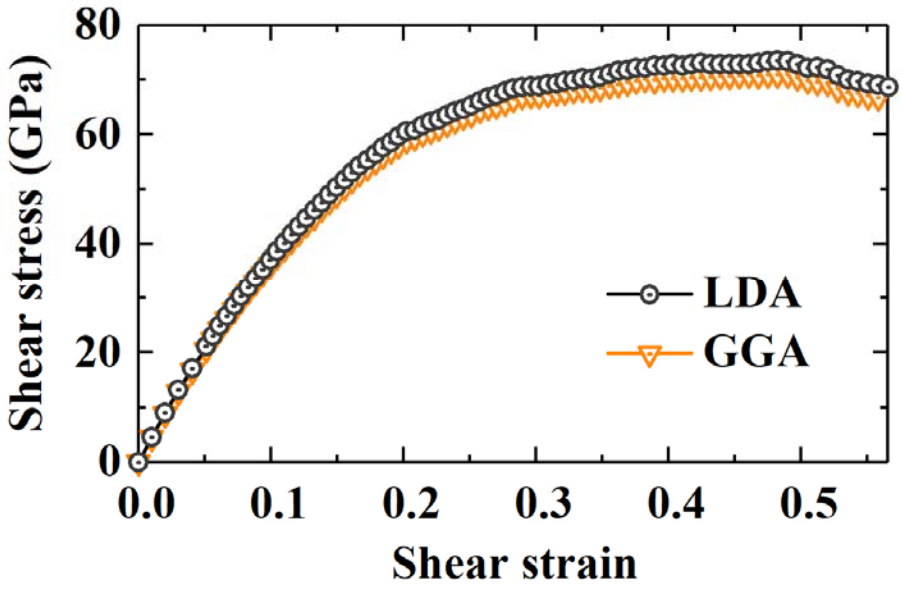

Fig. S1. Stress response of diamond under the (11-2)[111] constrained shear (CS) strains using the LDA or GGA functional, which are commonly employed to describe covalent materials like diamond. A normal-to-shear stress ratio of 2.475 is maintained during CS deformation, corresponding to biaxial stress under Vickers indentation. The two sets of stress responses of deformed diamond up to the dynamically stable limit are nearly identical in both the stress values and the range of dynamical stability determined by phonon calculations, indicating that our calculated stress response results are insensitive to the choice of exchange-correlation functional (LDA or GGA). It is seen that the GGA results are slightly below the LDA results, which is consistent with the established knowledge that LDA/GGA tends to overbind/underbind, leading to the stiffer/softer stress response as reflected in our calculated results.

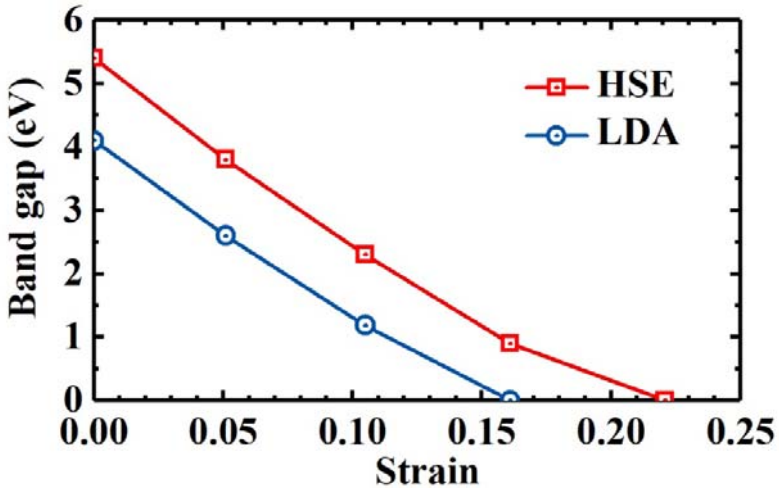

Fig. S2. Calculated electronic band gap of the CS deformed diamond using the LDA or HSE functionals.

To better describe the CS strain induced electronic band-gap closure, we have employed the HSE hybrid functional [5,6] with 25% Hartree–Fock exchange mixing to obtain more accurate band gaps for the exploration of metallization in strained diamond. As the strain increases, both the LDA and HSE calculations predict that the size of the band gap exhibits a negative strain dependence, and the metallization occurs at CS strain of 0.161 and 0.221, respectively, resulting in a small (~0.060) downshift of strain where strain-induced metallization occurs. In other words, an "effective strain" of 0.060 is advanced by the LDA calculation for the evaluation of band gap in the semiconducting regime of deformed diamond.

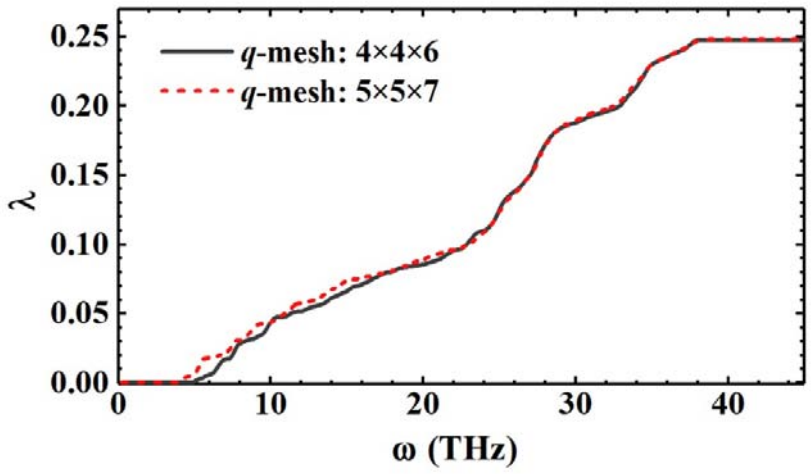

Fig. S3. The q-mesh convergence test for the calculated λ(ω) at a selected strain of 0.446 in the deformed diamond.

We used an 8-atom cell to calculate the electron-phonon coupling parameter in the deformed diamond. Under strain, deformed diamond crystal exhibits progressively reduced symmetry that leads to a substantially increased number of irreducible q points in the electron-phonon calculations; e.g., the number of irreducible q-points within the 4×4×6 q-mesh is 34 at smaller strains (ε = 0.283, 0.349, 0.446), but this number increases to 52 at larger strains (ε = 0.520, 0.566) due to the deformation induced reduction of symmetry. We checked the convergence of q-mesh in the electron-phonon calculations in deformed diamond. A 4×4×6 q-mesh yields electron-phonon coupling parameter convergence to within 0.001. In Fig. S3, we show the calculated λ(ω) at ε = 0.446 with 4×4×6 and 5×5×7 q mesh, with 34 and 54 irreducible q points at smaller strains, respectively. The calculated results with different q-mesh choices are in excellent agreement, and the difference of the obtained integrated λ values, which directly determines the Tc values, is less than 0.001. This outcome confirms that the q-mesh used in the present work is adequate to provide a reliable description for the phonon-mediated superconductivity in deformed diamond.

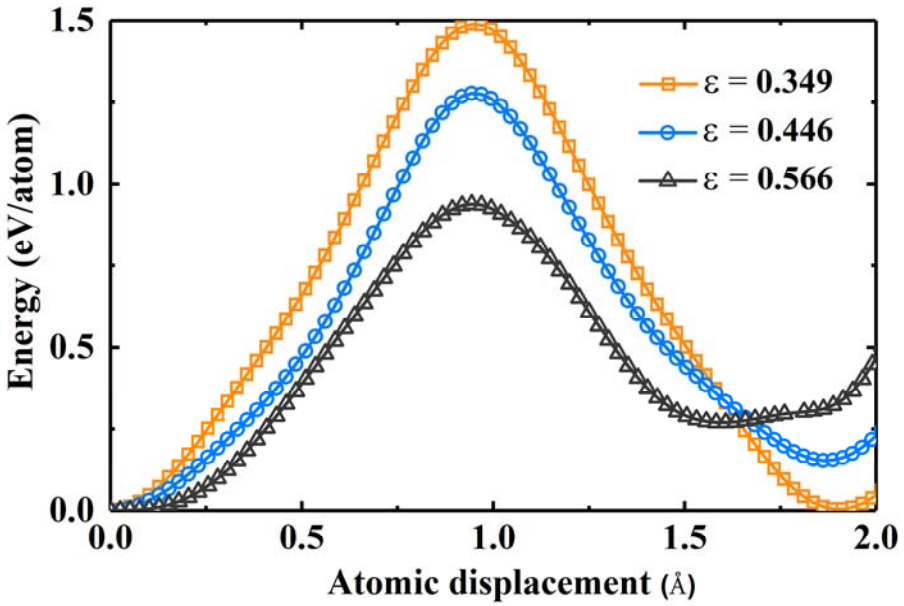

Fig. S4. Calculated energy evolution with atomic displacement in deformed diamond at CS strains of 0.349, 0.446, and 0.566. Here the atoms move along the paths of the vibrational eigenvectors of the most rapidly softening phonon modes at the A point in the Brillouin zone. The obtained substantial energy barriers indicate that the deformed diamond crystal, which remains dynamically stable based on phonon calculations, retains fairly robust structural integrity and viability at these large strains, making it feasible for experimental realization and exploration, despite technical challenges due to its closeness to the ductile structural failure under further deformation. In practice, delicate and skillful strain engineering manipulations are required to reach, monitor and probe such ultimately strained crystal structures and the associated properties. Some experimental efforts may encounter failure and multiple attempts may be needed to achieve the research objective, which is the case for current extreme-high-pressure experiments where anvil failures routinely occur and many attempts are required to reach the desired pressure range and obtain the corresponding measurement results. Such scenarios are part of exploring material behaviors under extreme physical (e.g., pressure/stress) conditions. Since our predicted superconducting behaviors in deformed diamond exist in a fairly wide CS stress/strain range, it is expected that it is feasible to detect this novel phenomenon in realistic experimental settings.

References

[1] E. S. Zouboulis, M. Grimsditch, A. K. Ramdas, and S. Rodriguez, Phys. Rev. B **57**, 2889 (1998).

[2] D. M. Teter, MRS Bull. **23**, 22 (1998).

[3] D. M. Ceperley and B. J. Alder, Phys. Rev. Lett. **45**, 566 (1980).

[4] J. P. Perdew, K. Burke, and M. Ernzerhof, Phys. Rev. Lett. **77**, 3865 (1996).

[5] J. Heyd, G. E. Scuseria, and M. Ernzerhof, J. Chem. Phys. **118**, 8207 (2003).

[6] J. Heyd, G. E. Scuseria, and M. Ernzerhof, J. Chem. Phys. **124**, 219906 (2006).